

## **A two-dimensional simulation of grain structure growth within substrate and fusion zone during direct metal deposition**

### **Abstract**

In this paper, a predictive model based on a cellular automaton (CA)-finite element (FE) method has been developed to simulate thermal history and microstructure evolution during metal solidification for a laser-based additive manufacturing process. The macroscopic FE calculation that is validated by thermocouple experiment is designed to update the temperature field and a high cooling rate. A cellular automata-finite element (CAFE) method is developed to describe grain growth in the fusion zone. In the mesoscopic CA model, heterogeneous nucleation sites, grain growth orientation and rate, epitaxial growth, remelting of preexisting grains, metal addition, grain competitive growth, and columnar to equiaxed phenomena were simulated. The developed “decentered polygon” growth algorithm is appropriate for the non-uniform temperature field. Finally, the single and multiple layer direct metal deposition (DMD) experiment is conducted to validate the characteristics of grain features in the simulation.

### **1 Introduction**

Compared with the conventional subtractive manufacturing technologies, additive manufacturing (AM) has unique advantages including low heat input, small heat-affected zone, solid-free-form fabrication, near-net-shape, and so on. Direct Metal Deposition (DMD), a rapid developing AM technique, is able to manufacture a fully dense metal part without intermediate steps, which is especially appropriate for the heterogeneous components manufacturing. During the deposition process, solidification thermodynamics determined by a series of process parameters affect microstructure evolution, which directly affects materials mechanical properties. The temperature field history and the cooling rate is the key factor to controlling the solidification microstructure after DMD process [1]. Several approaches, including stochastic and deterministic, have been taken to model solidification microstructure evolution. Anderson et al. [2][3] developed a Monte Carlo (MC) stochastic method to simulate the grain growth, topology, grain size distribution, curvature and grain velocities, as well as their interrelationships. Saito and Enomoto [4] incorporated the anisotropy of the grain boundary energy, the pinning effect of precipitates on growth kinetics into the MC simulation. Another idea of modeling is the deterministic approach. Chen [5] investigated a phase field (PF) method to model and predict mesoscale morphological and microstructure evolution in materials. Krill et al. [6–8] developed PF to simulate 2D grain growth, 3D gain growth, equiaxed solidification. However, a phase field model usually carries a very high computational cost because of a requirement for a particularly fine computational grid.

In order to reduce the computational cost, RAPPAZ and GANDIN [9] put forward a two dimensional cellular automaton approach to model the grain structure formation in the solidification process. The model includes the mechanisms of heterogeneous nucleation and of grain growth. Nucleation occurring at the interface as well as in the liquid metal is treated by using two distributions of nucleation sites. The location and the crystallographic orientation of the grains are chosen randomly among a large number of cells and a certain number of orientation classes, respectively. However, the model was then applied to small Al–7wt%Si specimens of uniform temperature. In order to develop the non-uniform temperature prediction, GANDIN et al [10] proposed a 2-dimensional Cellular Automaton (CA) technique for the

simulation of dendritic grain formation during solidification. The non-uniform temperature situation was fully coupled to an enthalpy-based Finite Element (FE) heat flow calculation. This progress made it possible to combine the temperature field history with the microstructure evolution. The coupled CA-FE model is applied to Al-7wt% Si alloy. A three dimensional CA-FE model was analyzed of prediction of dendritic grain structures formed during solidification [11]. The potentiality of the CA-FE model is demonstrated through the predictions of typical grain structures formed during the investment casting and continuous casting processes. Based on the features of several developing approaches, Choudhury et al [12] compared a CA model with a PF model for simulations of dendritic solidification of an Al-4wt%Cu alloy, two- and three-dimensionally at different undercooling. In 2D, the PF model shows an excellent agreement of the simulated tip properties. At high undercooling, the CA model becomes advantageous, as its reproduction of the theoretical behavior improves. As the CA model is capable of simulating at coarse scales in a comparably short time, its output can be used as input for a PF simulation for resolving finer details of microstructure formation. This can be utilized to build a hybrid model to integrate CA high efficiency and PF accuracy. Dore [13] investigated quantitative prediction of micro-segregation during solidification of the ternary alloy system, which is applied to solidification of Al-Mg-Si. Jarvis et al [14] firstly compared 1D, 2D and 3D cellular automaton finite difference (CA-FD) simulations of non-equilibrium solidification in Al-3.95Cu-0.8Mg ternary alloy. It has been demonstrated that there is good agreement between all CA-FD models in terms of primary  $\alpha$ -Al phase. However, final dendrite arm spacings of 2D and 3D are slightly overestimated.

High cooling rate and non-equilibrium is a typical characteristic of DMD technique comparing conventional casting process and simulation. Grujicic et al. [15] proposed a modified CA-based method to investigate the evolution of solidification grain microstructure during LENS rapid fabrication process. This research established the relationship between process parameters (e.g. laser power, laser velocity) and solidification microstructure in binary metallic alloy. The finite difference analysis was also coupled with the modified CA to calculate the temperature field as the input of microstructure prediction. Kelly et al. [16][17] developed the thermal history in DMD of Ti6Al4V and microstructural characterization.

In this study, ABAQUS was used to calculate the temperature field of the whole part, which offers the macroscopic FE nodes' temperature. Interpolation was utilized to obtain the finer nodes' temperature based on the FE nodes result. The temperature field was validated by the type K thermocouples. The CA model was built to simulate the microstructure information, such as the grain size and columnar grain orientation. The developed "decentered polygon" algorithm is more appropriate for grain structure development in the non-uniform temperature field. This simulation will lead to new knowledge that simulates the grain structure development of single-layer and multiple-layer deposition during DMD process. The microstructure simulation results were validated by the experiment. The model parameters for the simulations were based on Ti-6Al-4V material.

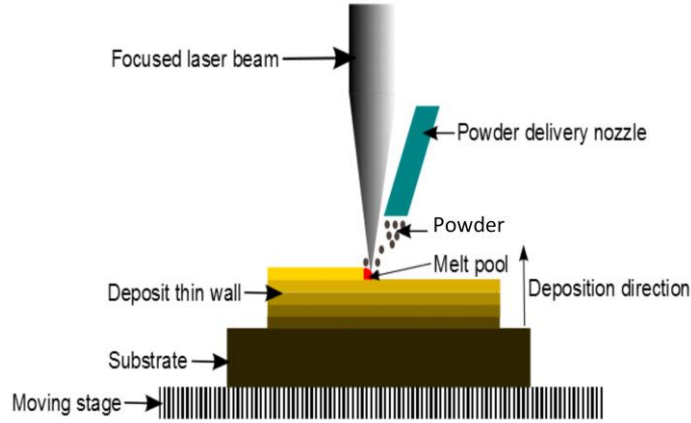


Figure 1. Laser Powder Deposition Schematic

## 2 Mathematical model

### 2.1 Ti6Al4V transient temperature field during the deposition process

In the Direct Metal Deposition (DMD) process, the temperature history of the whole domain directly influences the deposition microstructure, which is critical to mechanical properties [18]. In order to obtain the microstructure information during the solidification process, the temperature field must be known at each time step. The transient temperature field throughout the domain was obtained by solving the 3D heat conduction Eq (1), in the substrate, along with the appropriate initial and boundary conditions [19].

$$\rho(T) \cdot c_p(T) \cdot \frac{\partial T}{\partial t} = \frac{\partial}{\partial x} \left( k(T) \frac{\partial T}{\partial x} \right) + \frac{\partial}{\partial y} \left( k(T) \frac{\partial T}{\partial y} \right) + \frac{\partial}{\partial z} \left( k(T) \frac{\partial T}{\partial z} \right) + \dot{Q}, \quad (1)$$

where  $T$  is the temperature,  $\rho(T)$  is the density,  $c_p(T)$  is the specific heat,  $k(T)$  is the heat conductivity, and  $Q$  is the internal heat generation following certain energy distribution per unit volume.

The initial conditions applied to solve Eq (1) were:

$$T(x, y, z, 0) = T_0 \text{ and } T(x, y, z, \infty) = T_0, \quad (2)$$

where  $T_0$  is the ambient temperature. In this study,  $T_0$  was set as room temperature, 298 K. The boundary conditions, including thermal convection and radiation, are described by Newton's law of cooling and the Stefan-Boltzmann law, respectively. The laser heating source term,  $\dot{Q}$  in Eq (1), also was considered in the boundary conditions as a surface heat source. The boundary conditions then could be expressed as [19]

$$K(\Delta T \cdot n)|_{\Gamma} = \begin{cases} [-h(T - T_0) - \varepsilon(T)\sigma(T^4 - T_0^4)]|_{\Gamma} & \Gamma \notin \Lambda \\ [Q - h(T - T_0) - \varepsilon(T)\sigma(T^4 - T_0^4)]|_{\Gamma} & \Gamma \in \Lambda \end{cases} \quad (3)$$

where  $k$ ,  $T$ ,  $T_0$  and  $Q$  bear their previous definitions,  $n$  is the normal vector of the surface,  $h$  is the heat convection coefficient,  $\varepsilon(T)$  is the emissivity,  $\sigma$  is the Stefan-Boltzman constant which is  $5.6704 \times 10^{-8} \text{ W/m}^2\text{K}^4$ ,  $\Gamma$  represents the surfaces of the work piece and,  $\Lambda$  represents the surface area irradiated by the laser beam.

In order to simulate the thermal history during the Direct Metal Deposition more efficiently and reduce the computational cost, some assumptions were taken into account. In the experiment, a Gaussian distributed laser beam was utilized to melt the substrate vertically with a non-uniform power density. [20] Thus, the transverse intensity variation is described as Eq (4):

$$I(r, y) = \alpha \frac{P}{\pi w(y)^2/2} \exp\left(-2 \frac{r^2}{w(y)^2}\right), \quad (4)$$

where  $\alpha$  is the laser absorption coefficient,  $P$  is the power of the continuous laser, and  $w(y)$  is the distance from the beam axis where the optical intensity drops to  $1/e^2 (\approx 13.5\%)$  of the value on the beam axis.  $\alpha$  was set as 0.4 based on numerical experiments in the LAMP lab, and  $w(y)$  is 1 mm in this simulation. The motion of laser beam was simulated by adjusting the position of beam center  $R$  with programming a user subroutine “DFLUX” in ABAQUS. The formula of  $R$  is as follows:

$$R = \left[ \left( x - \int_{t_0}^t u dt \right) + \left( y - \int_{t_0}^t v dt \right) + \left( z - \int_{t_0}^t w dt \right) \right]^{1/2}, \quad (5)$$

where  $x$ ,  $y$ , and  $z$  are the spatial coordinates of the Gaussian laser beam center, and  $u$ ,  $v$ , and  $w$  are the laser moving velocities.

The Marangoni effect caused by the thermocapillary phenomena can directly influence the temperature field in the whole domain, so it is taken into account to obtain more accurate thermal history during DMD. [21] The artificial thermal conductivity was put forward to addressing the Marangoni effect in the finite element method [22]

$$k_m(T) = \begin{cases} k(T), & T \leq T_{liq} \\ 2.5k(T), & T > T_{liq} \end{cases}, \quad (6)$$

where  $k_m$  is the modified thermal conductivity, and  $T_{liq}$  is the liquidus temperature.

In the FEA model, the powder addition was simulated by activating elements in many small steps.[23] The width of the deposit area is assumed to be the same as the Gaussian laser beam. The thickness of each layer is calculated by transverse speed, powder feed rate and powder absorption efficiency. The deposit geometry, boundary condition and heat flux was updated after each step.

Figure 15 depicts the temperature field of the substrate and deposited material, including the 25-layer deposition materials added on the substrate when the laser moved forward and backward. The laser deposition of multiple-layer Ti-6Al-4V was conducted with the power of 750 W, scanning speed of 200 mm/min, and powder delivery of 2 g/min. The elemental size is

non-uniform along three directions since it is not necessary to apply fine elements to where the location is far from the molten pool. Figure 15 shows that the thermal history and peak temperature of different layers are not identical. The higher layer performs higher thermal history because the higher layer accumulates more heat than the lower one and it is closer to heat source.

## 2.2 Ti6Al4V morphology prediction after solidification

Heterogeneous nucleation occurs nearly instantaneously at a characteristic undercooling. The locations and crystallographic orientation of the new nuclei are randomly chosen at the surface or in the liquid. As explained by Oldfield [24], the continuous nucleation distribution,  $dn/d\Delta T'$ , which characterizes the relationship between undercooling and the grain density, is described by a Gaussian distribution both at the mould wall and in the bulk liquid. The parameters of these two distributions, including maximum nucleation density  $n_{max}$ , the mean undercooling  $\Delta T_N$ , and the standard deviation of the grain density distribution  $\Delta T_\sigma$ , can be obtained from experiments and grain size measurements. The grain density,  $n(\Delta T)$ , is given by Eq (7):

$$\begin{aligned} n(\Delta T) &= \int_0^{\Delta T} \frac{dn}{d\Delta T'} d\Delta T' \\ &= \int_0^{\Delta T} \frac{n_{max}}{\Delta T_\sigma \sqrt{2\pi}} \exp\left[-\frac{1}{2}\left(\frac{\Delta T' - \Delta T_N}{\Delta T_\sigma}\right)^2\right] d\Delta T', \end{aligned} \quad (7)$$

where  $n_{max}$  is the maximum nucleation density of nucleation grains, which is obtained by the integral of the nucleation distribution (from zero undercooling to infinite undercooling).  $\Delta T_N$  and  $\Delta T_\sigma$  are the mean undercooling and standard deviation of the grain density distribution, respectively. Here, all temperatures are in Kelvin.

Undercooling is the most important factor in the columnar and dendrite growth rate and grain size. The total undercooling of the dendritic tip consists of three parts: solute undercooling, thermal undercooling, and curvature undercooling. For most metallic alloys, the kinetic undercooling for atom attachment is small, so it is neglected [25]. The total undercooling can be calculated as follows:

$$\Delta T = mC_0[1 - A(P_c)] + \theta_t I(P_t) + \frac{2\Gamma}{R}, \quad (8)$$

where  $m$  is the liquidus slope;  $\Gamma$  is the Gibbs-Thomson coefficient;  $C_0$  is the solute concentration in the liquid far from the solid-liquid interface;  $P_t$  and  $P_c$  are the thermal and solutal Peclet numbers, respectively;  $k$  is the solute partition coefficient at the solid-liquid interface;  $A(P_c)$  equals  $[1 - (1 - k)I(P_c)]^{-1}$ ;  $\theta_t$  is the unit thermal undercooling ( $= \Delta h_f/c$ ); and  $R$  is the radius of the dendritic tip.

For the laser deposition process, the rapid solidification condition corresponds to a high Peclet number at which the dendritic tip radius is given by Eq (9)

$$R = \left[ \frac{\Gamma}{\sigma^*(mG_c^* - G^*)} \right]^{1/2}, \quad (9)$$

where  $\sigma^*$ , the marginal stability constant, approximately equals  $1/4\pi^2$  [26], and  $G^*$  and  $G_c^*$  are the effective temperature gradient and concentration gradient, respectively.

### 2.3 Coupling Macroscopic FE and Mesoscopic CA Models

The temperature field result can be used to calculate enthalpy increment, which is necessary to calculate enthalpy at each time step. A linearized implicit FE enthalpy formulation of the heat flow equation can be given by Ref [10]

$$\left[ \frac{1}{\Delta t} \cdot [M] + [K]^t \left[ \frac{\partial T}{\partial H} \right]^t \right] \cdot \{\delta H\} = -\{K\}^t \cdot \{T\}^t + \{b\}^t, \quad (10)$$

where  $\{M\}$  is the mass matrix;  $\{K\}$  is the conductivity matrix;  $\{b\}$  is the boundary condition vector; and  $\{T\}$  and  $\{H\}$  are the temperature and enthalpy vectors at each node of the FE mesh, respectively. The Newton Method and Euler implicit iteration are included in (10). This set of equations can be solved using the Gauss elimination method for  $\{\delta H\}$ .

$$\delta H = \rho \cdot c_p \cdot [T^{t+\delta t} - T^t] - \Delta H_f \cdot \delta f_s. \quad (11)$$

Thus, the next time-step enthalpy can be obtained by the relationship of  $H_i^{t+1} = H_i^t + \delta H$ . The new temperature field can be obtained from the coupling model using (11).  $\Delta H_f$  is the latent heat of fusion per unit volume.  $f_s$  represents the fraction of solid.  $\delta f_s$  can be calculated as in [10].

In the FE macroscopic model, the temperature field was calculated on a relatively coarse mesh, but the solidification microstructure had to be developed on a finer regular CA mesh with a cell size of the order of the secondary dendrite arm spacing (SDAS). Figure 2 indicates the interpolate relationship between coarse FE nodes and fine CA cells. The known temperature  $T_n^t$  and the volumetric enthalpy variation  $\delta H_n$  were interpolated into the CA network by the linear interpolation in Eq (12) and (13).  $\phi_{vn}$  is the interpolation coefficient. Every CA cell temperature in the calculation domain can be obtained with this interpolation.

$$T_v^t = \sum_n \phi_{vn} \cdot T_n^t \quad (12)$$

$$H_v^t = \sum_n \phi_{vn} \cdot H_n^t \quad (13)$$

The finer temperature,  $T_v^t$ , and enthalpy variations  $\delta H_v^t$  in regular CA cells were used in Eq (13) to yield the temperature in the next micro time step. After a few micro time steps, the temperature field in the CA network could be substituted into the coarser nodes of the macroscopic model. The interpolated temperature field is employed as the model input. Heterogeneous nucleation, grain growth orientation, and grain growth are solved in the CA-FE model in terms of nucleation location distribution, random crystallographic orientation, and CA

cells capture. Figure 3 indicates the flow chart of coupling FE-CA model. The details of CA growth algorithm are shown in Figure 4. The transition rules for all CA cells are shown in Table 1.  $I_i$  denotes the cell  $i$  state before transition.  $T_i$  and  $T_L$  denotes the temperature of cell  $i$  before transition and liquidus temperature.

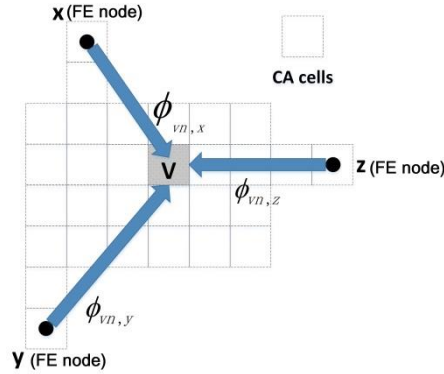


Figure 2.  $x$ ,  $y$ , and  $z$  represents the FE temperature nodes (coarse grids), and  $v$  represents the CA cells (fine grids). The three linear interpolation coefficients from FE nodes  $x$ ,  $y$ ,  $z$  to CA cells  $v$  are  $\phi_{vn,x}$ ,  $\phi_{vn,y}$  and  $\phi_{vn,z}$

Figure 5 illustrates the conventional and modified cell capture algorithm. For the conventional method, the growth of the square envelope is determined by the center cell temperature at this time step, which results in the same growth rate for the four vertices. The modified “Decentered Polygon” algorithm is implemented to control the grain growth within melt pool and at the solid/liquid interface. Compared to the traditional “decentered square” algorithm of cell capturing, the modified “decentered polygon” algorithm does not need to create square for each cell when it begins to grow. Only the decentered polygon of a starting nucleated cell is tracked during the grain growth process, which reduces the computation cost. Besides, the modified algorithm can prevent grain orientations from realigning with  $x$  axis after a few growing steps because each cell will stop growing when Von Neumann and Moore neighbors are both solid. The controlling point growth rate is determined by the local cell temperature. Therefore, the region with higher thermal gradient will solidify faster along the steepest thermal gradient.

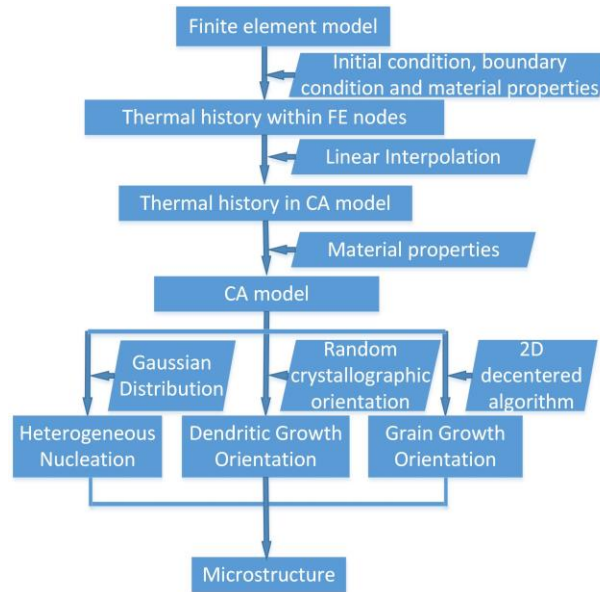


Figure 3. Flow chart of coupling FE-CA model.

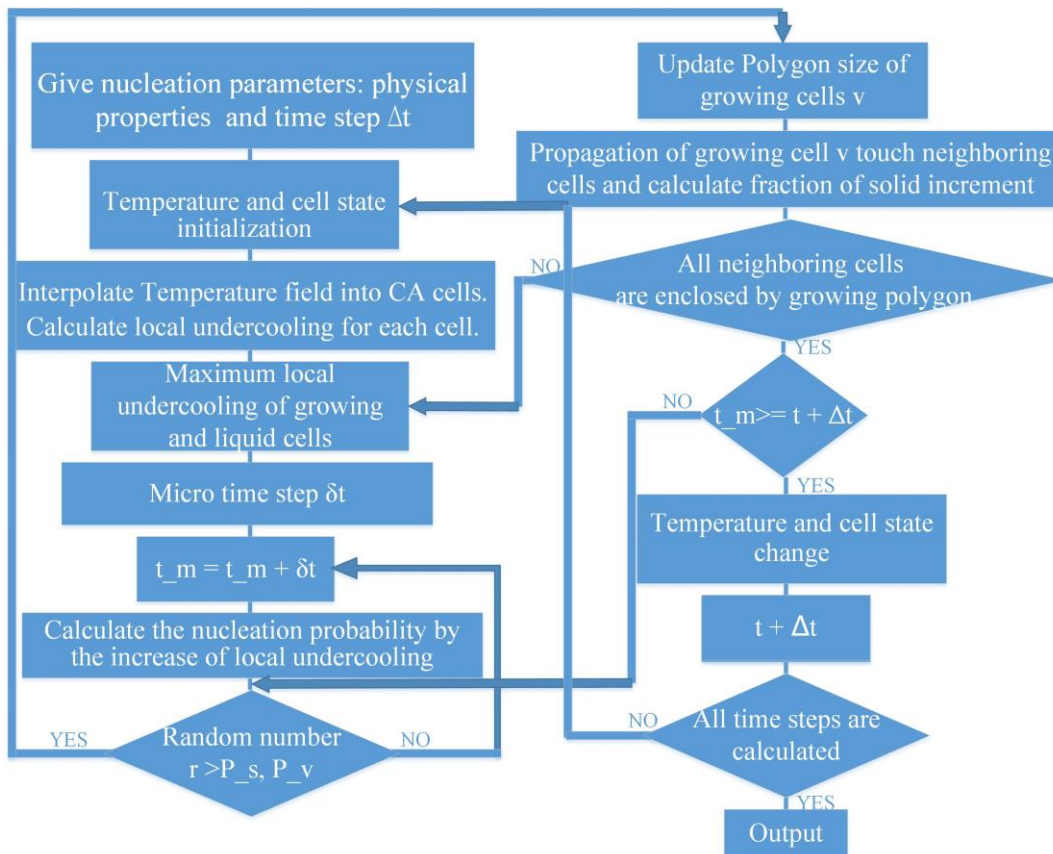


Figure 4. Flow chart of algorithm of cellular automaton

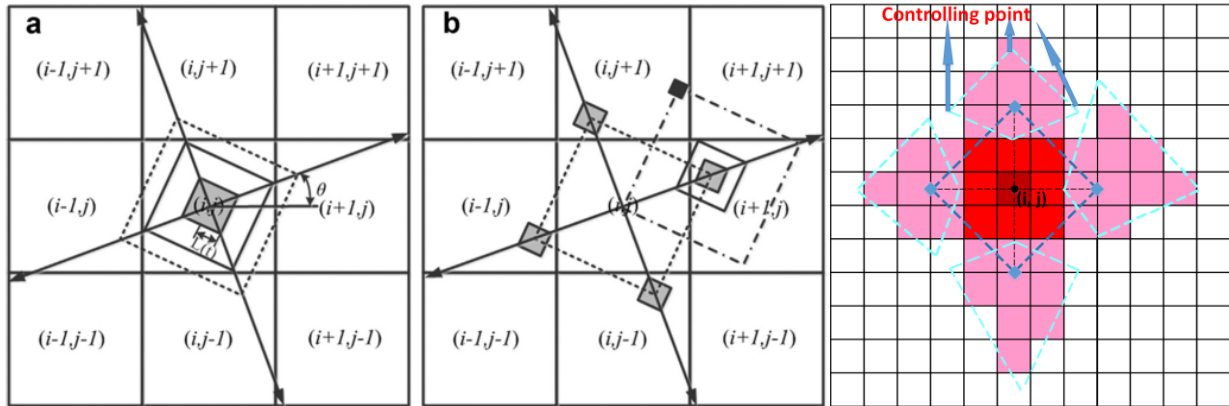


Figure 5. Illustration of the conventional and modified cell capture algorithm: (a) capturing rule of cell (i, j) within a decentered square, (b) capturing rule of 8 neighboring cells before (i, j) growth termination [27], (c) the modified cell capture and growth algorithm of "Decentred Polygon" with neighboring cells effect for cubic crystal alloys.

Table 1. Transition rules for CA cells

Cell state before transtion	Transition condition	Cell state after transition	Stage
$I_i > 0$	$T_i > T_L$	$I_i = 0$	Melting
$I_i = 0$	A grain is nucleated in the ith cell	$I_i = 1$	Nucleation
$I_i = 0$	The ith cell is captured by a neighboring cell	$I_i = 1$	Capture
$I_i = 1$	The envelope centered at the ith cell has encompassed all the neighboring cells	$I_i = 2$	Growth

### 3 Results and Discussion

### 3.1 Single-layer temperature and grain structure

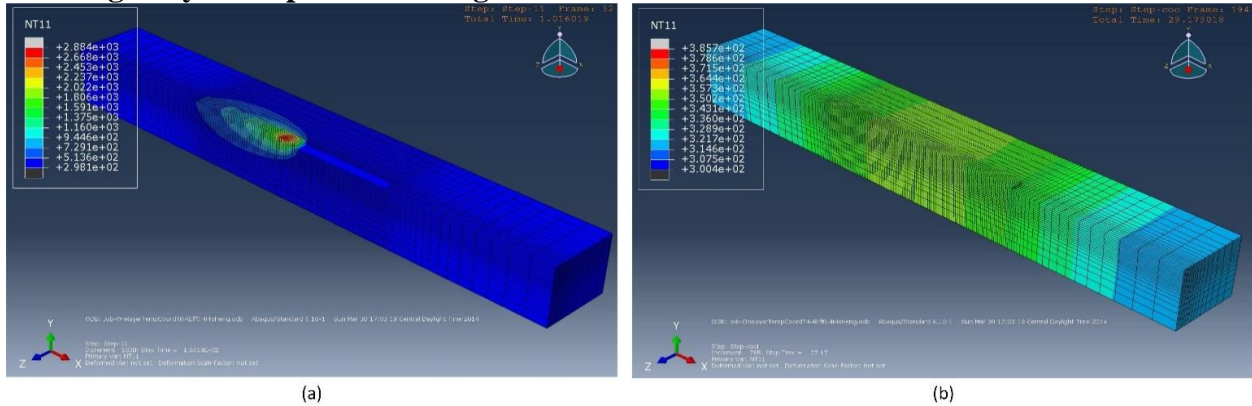
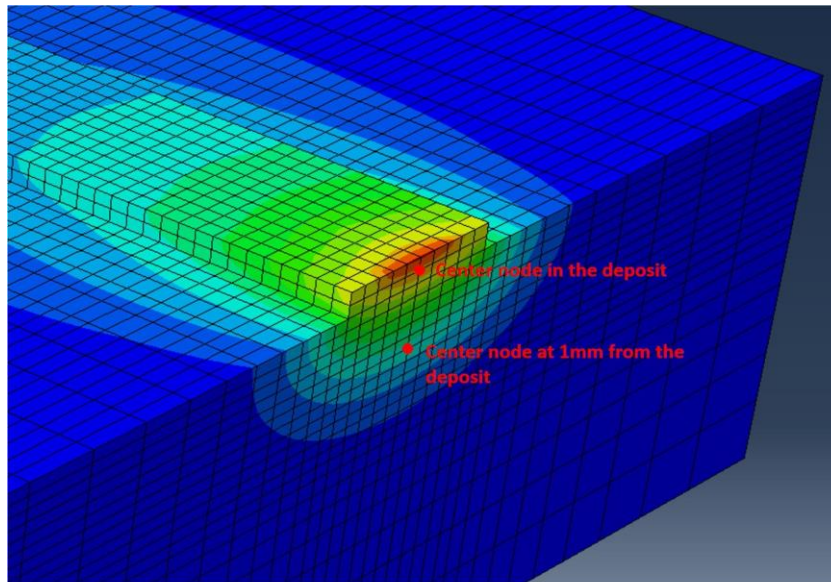


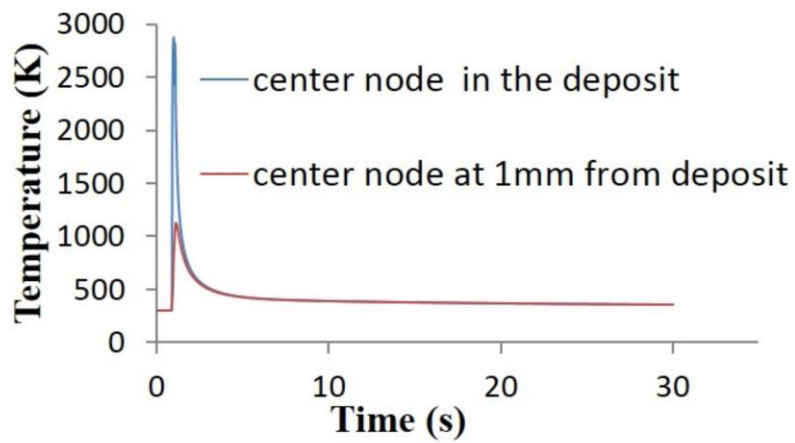
Figure 6. Cross sectional simulated temperature distribution during single-layer laser deposition process. The deposition time is 2s, while the cooling time is 28s. (a) Temperature field at time = 1.0s (b) Temperature field at time = 29.0s

The deposition temperature field and grain morphology were simulated first only in one layer. Figure 6 shows thermal history of the whole block during the DMD process. Figure 6(a) indicates the temperature field of the whole block when laser beam is passing along x direction at time = 1.0s, while Figure 6(b) shows the temperature field when substrate cools down with laser off at time = 29.0s. The total physical time of one-layer laser deposition is 2 s, while the cooling time is 28 s in the simulation. For each step, the step time is 0.1 s when the laser is shot on the surface of the deposited material. After 30 s cooling down, the temperature distribution is more uniform. Figure 7 indicates the thermal history of two nodes, which locate at the center point in the deposit and 1mm away from the deposit. The result shows that the highest temperature in the deposit is approximately 2884 K, which occurred at the center of the Gaussian beam. The center node at 1mm away from the deposit arrives at peak temperature of 1126K that cannot melt the Ti6Al4V substrate. Based on every node's thermal history, the undercooling (discrepancy between liquidus temperature and current temperature) that is critical to resulting in grain nucleation and growth rate can be determined.

In order that the input of microstructure model is reliable, the temperature field is validated with four type K thermocouples. The locations are shown in Figure 8. One is located at the starting end of laser path. Another three points are located by one side of laser path. Arduino device is used to sample the temperature data. The TC position is near to the melt pool. The distance is 3 ~ 3.5mm. A laser deposition experiment is conducted with the power of 750 W, scanning speed of 600 mm/min and 2g/min for single-layer deposit. The difference between experiment and FEM modeling is less than 10 Celsius degree shown in Figure 9. In the real experiment, the substrate is fixed by the metal fixture, which resulting in the more heat conduction than the FEM model. Because of argon gas, forced convection occurred in the real experiment. This also cause lower cooling rate in the temperature simulation. Because the difference between experiment and simulation is smaller than 10%, the current FEA modeling is still considered as a reasonable simulation of temperature field, which can provide the reliable thermal input for the CA model.



(a)



(b)

Figure 7. Temperature history at the center node in the deposit and substrate during deposition and cooling process

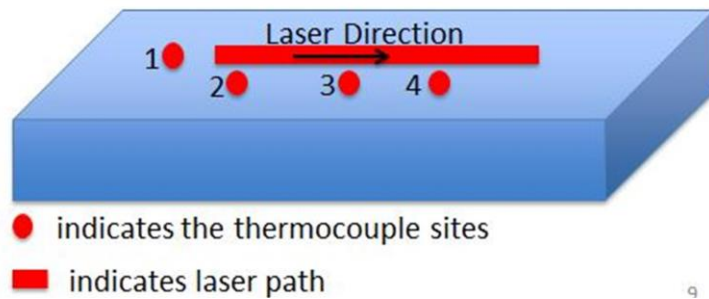
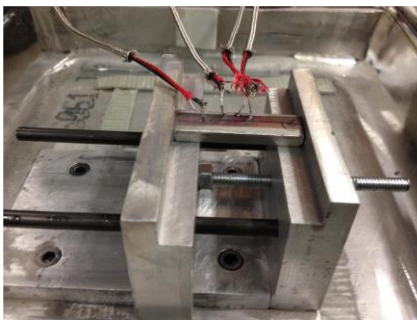


Figure 8. Thermocouples location and laser scan direction schematic diagram

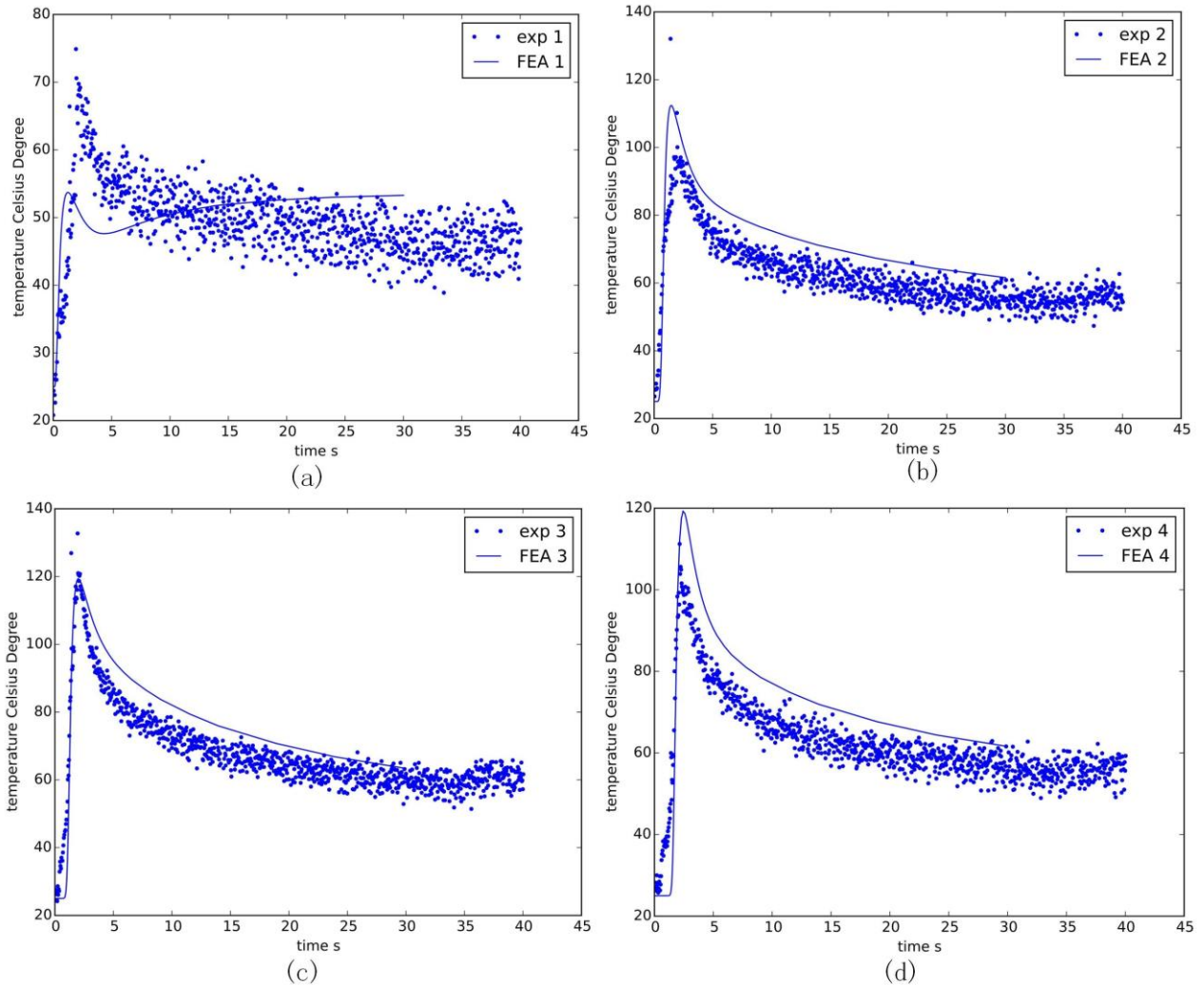


Figure 9. Temperature validation with four type K thermocouples. (a), (b), (c) and (d) are measured at location 1, 2, 3, and 4, respectively.

A laser deposition experiment is conducted with the power of 700 W, scanning speed of 600 mm/min and 2g/min for single-layer deposit. For this case, the cross section shown in the figure is the computational domain. The cell size for this simulation is  $6\mu\text{m} \times 6\mu\text{m}$ . X and Y axis represents the number of cell. The simulation result from conventional method is shown Figure 10. It can be observed that even though different grains own diverse orientation at the very beginning, the crystallographic orientation preference tend to be along the axis after several time steps. Here, different color represents various grain orientations. Finally, the equiaxed grains dominate the fusion zone. The original grain orientations are not kept during the solidification process. It doesn't agree well with the single-layer experimental result shown in Figure 12.

The developed CA grain growth method is implemented under the same condition. According to the developed CAFÉ simulation, the single layer simulation result is shown in Figure 11. The grain keeps its original crystallization orientation when grain growth is modelled. The

columnar grain can be identified from the solid/liquid interface. When grains continue to grow towards melt pool center, some grains overgrow other grains such that there are fewer grains further away from the solid/liquid interface.

Three samples of single-layer deposits are prepared with EDM cutting, grinding, polishing and etching. The optical microscope is shown in Figure 12. The comparison between simulation and experimental results are shown in Figure 13. An average of twenty measurements per sample is performed in order to determine the average grain size number. It compares the experimental average grain size number with the predicted average grain size number. The shown data suggests that a 15% error between measurements and predictions is present. This can be considered as a reasonable prediction of grain morphology and size.

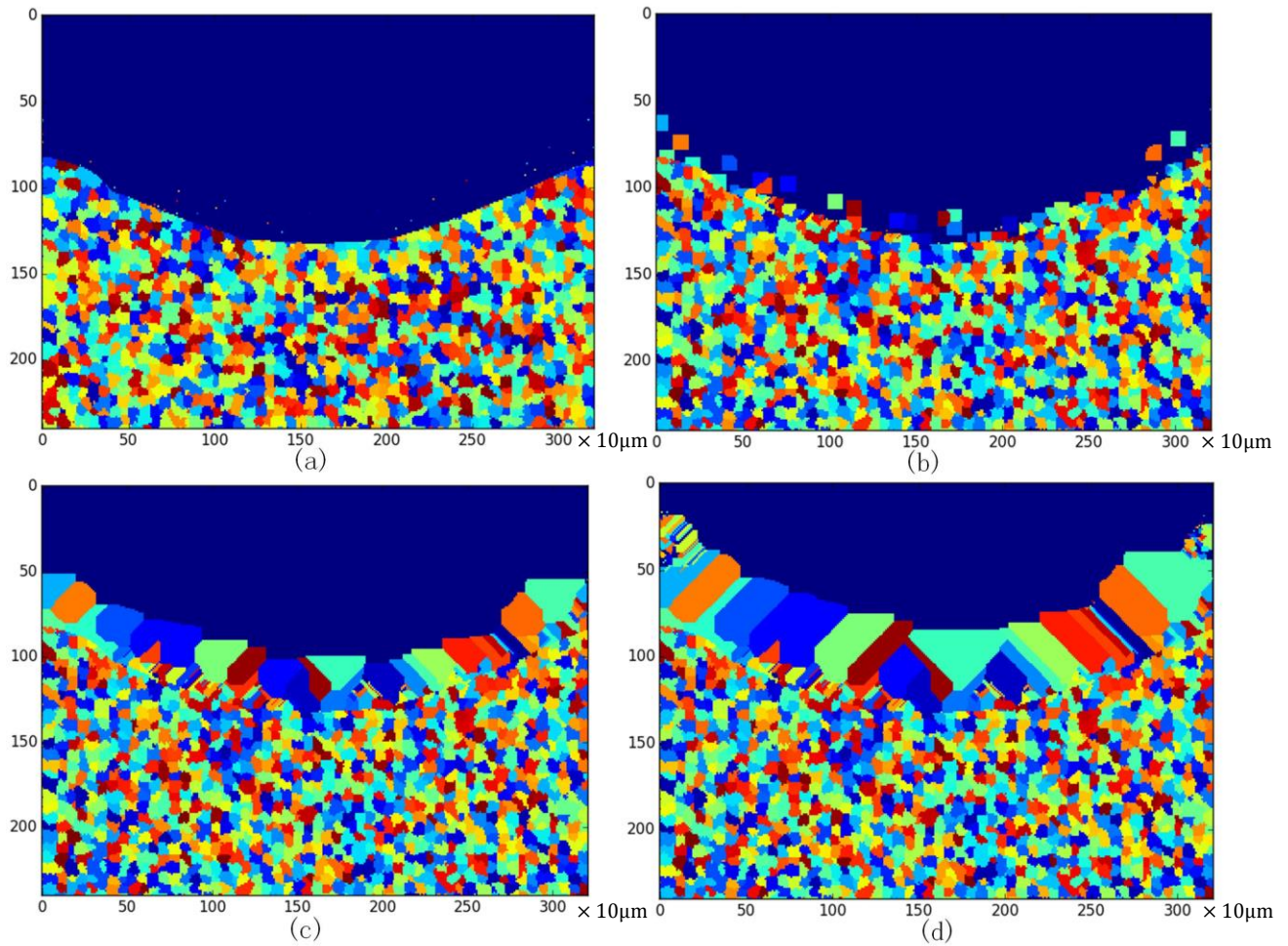


Figure 10. Grain structure of conventional growth method for single layer Ti6Al4V deposition

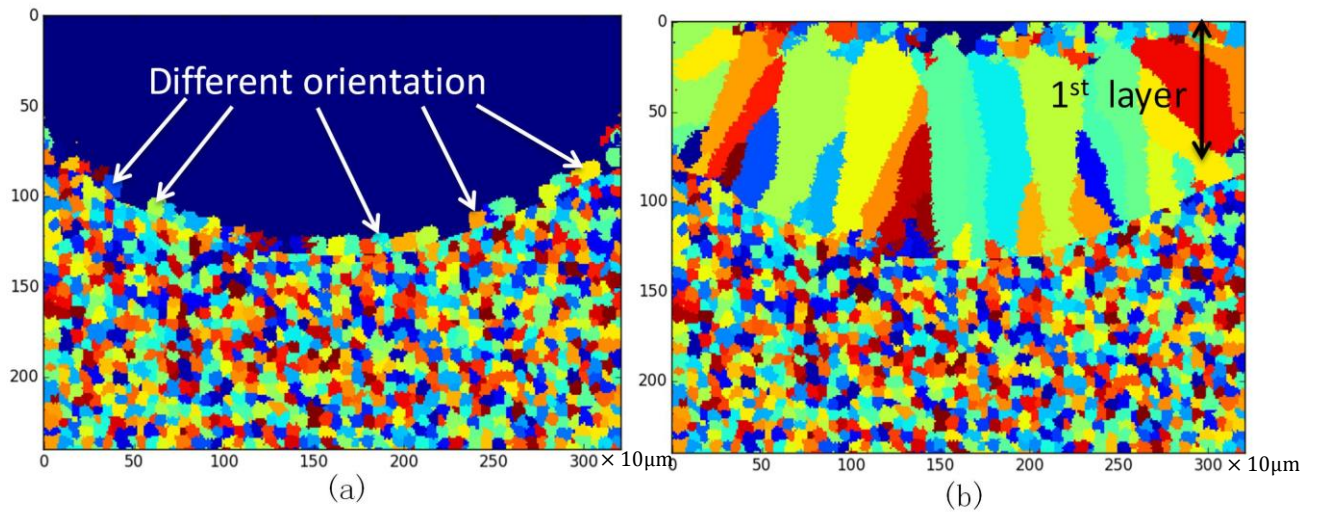


Figure 11. Grain structure of developed growth method for single layer Ti6Al4V deposition

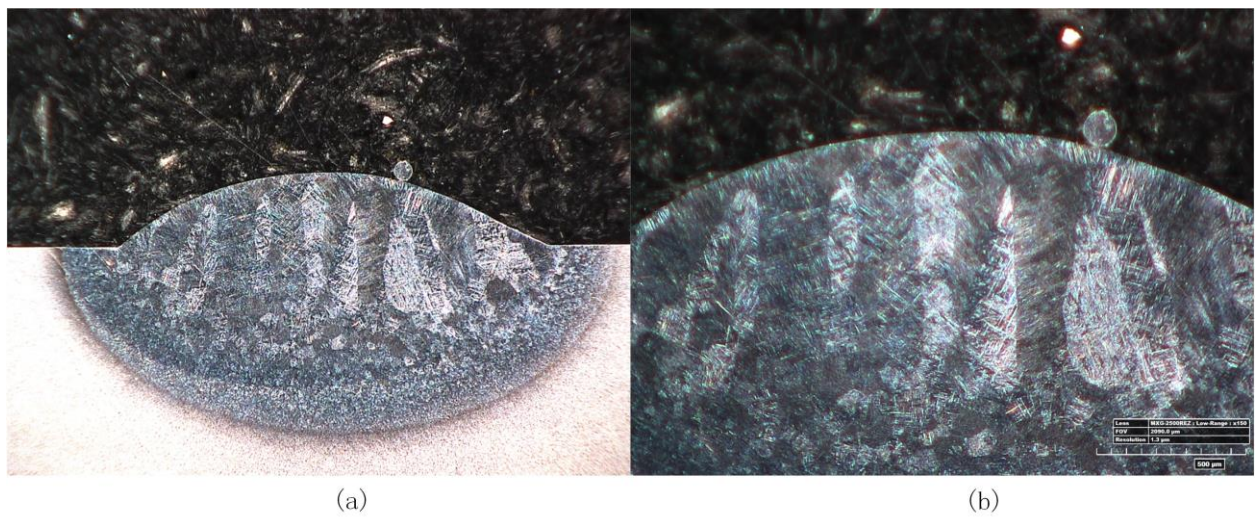


Figure 12. Ti-6Al-4V single-layer deposition grain morphology

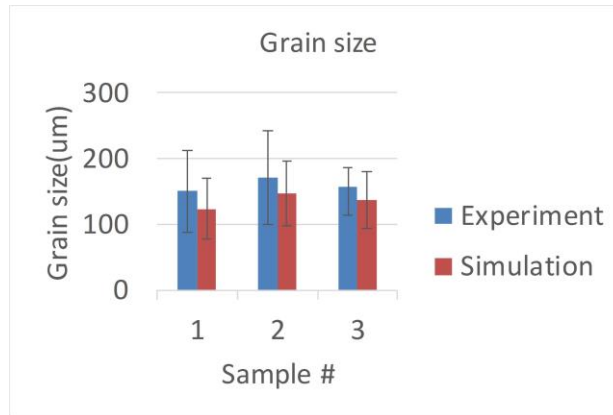


Figure 13. Grain size comparison between simulation and experiment

### 3.2 Multi-layer temperature and grain structure

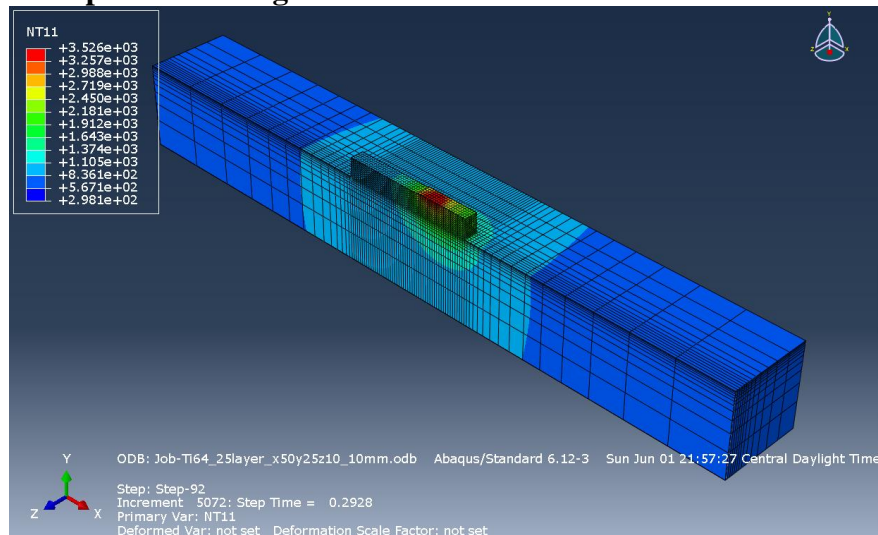


Figure 14. Thermal history for 25-layer Ti-6Al-4V laser deposition. The current figure shows the 18th layer deposit temperature field

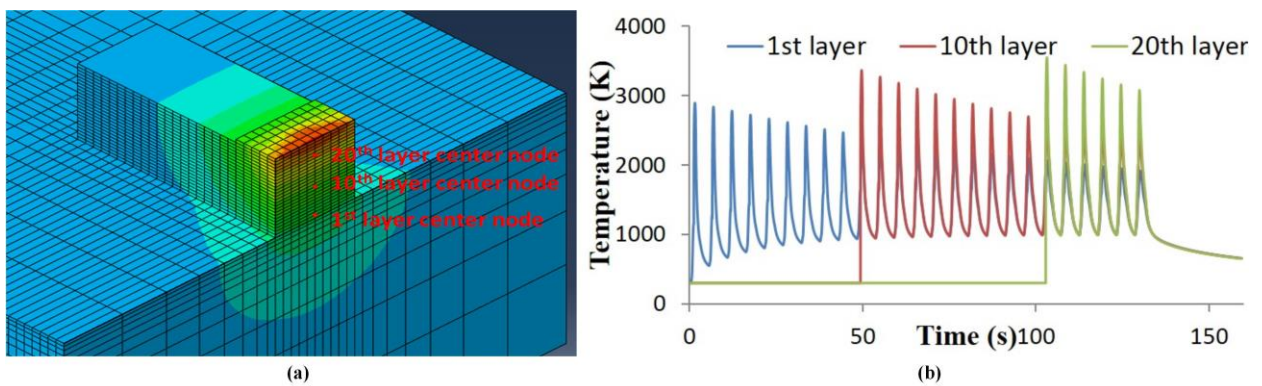


Figure 15. (a) Three nodes location cross-section schematic (b) Thermal history of the center node at 1st, 10th and 20th layer

Figure 14 depicts the temperature field of the substrate and deposited material, including the 25-layer deposition materials added on the substrate when the laser moved forward and backward. The laser deposition of multiple-layer Ti-6Al-4V was conducted with the power of 750 W, scanning speed of 200 mm/min, and powder delivery of 2 g/min. The powder absorption efficiency in the LAMP lab is about 0.3 – 0.4 after the measurement. The elemental size is non-uniform along three directions since it is not necessary to apply fine elements to where the location is far from the molten pool. Figure 15 shows that the thermal history and peak temperature of different layers are not identical. The higher layer performs higher thermal history because the higher layer accumulates more heat than the lower one and it is closer to heat source.

Figure 16 shows Ti-6Al-4V deposition grain microstructure. The deposit region cross section dimension is 1.8mm × 1.9mm, which is close to 2mm × 2mm assumption in the simulation. In Figure 16, it can be observed that at the bottom deposition, crystallographic orientation is not only limited to the vertical direction. It can be observed that columnar grains dominate in the laser deposition area. Figure 16(a) and (b) indicate the whole deposition region at different magnification and the locations of top and bottom region, while Figure 16(c) and (d) shows the grain size and shape with higher magnification. Under the same condition, the experiment is conducted and the optical microscope images are taken. Figure 16(e) shows multiple layers of the Ti-6Al-4V grain morphology under the laser deposition process. Irregular grain shape and size can be obtained. When more layers were deposited, prior  $\beta$  columnar grains began to dominate, while equiaxed grains began disappearing. As the solidification process continues, competitive growth among different grains occurs. Therefore, the size of columnar grain increases, and the number of grains goes down. The orientations of the columnar grains were almost perpendicular to the laser motion's direction because the grains grew along steepest thermal gradient direction. This phenomenon verifies the columnar grain orientation in the simulation result. The domain size in the CA model was 2 mm × 2 mm. After measurement of grain size, it can be found in Figure 17 that in the simulation, the grain size ranges from 113um to 346um. For the experiment, the grain size ranges from 156um to 599um. The grain size at the bottom and top are larger than the simulation. This may be because it doesn't consider the cyclic heating and cooling process effect on the solidified grain evolution. Usually cyclic heating will coarsen the grain and make the grain become larger. This effect should be solved in the future research task.

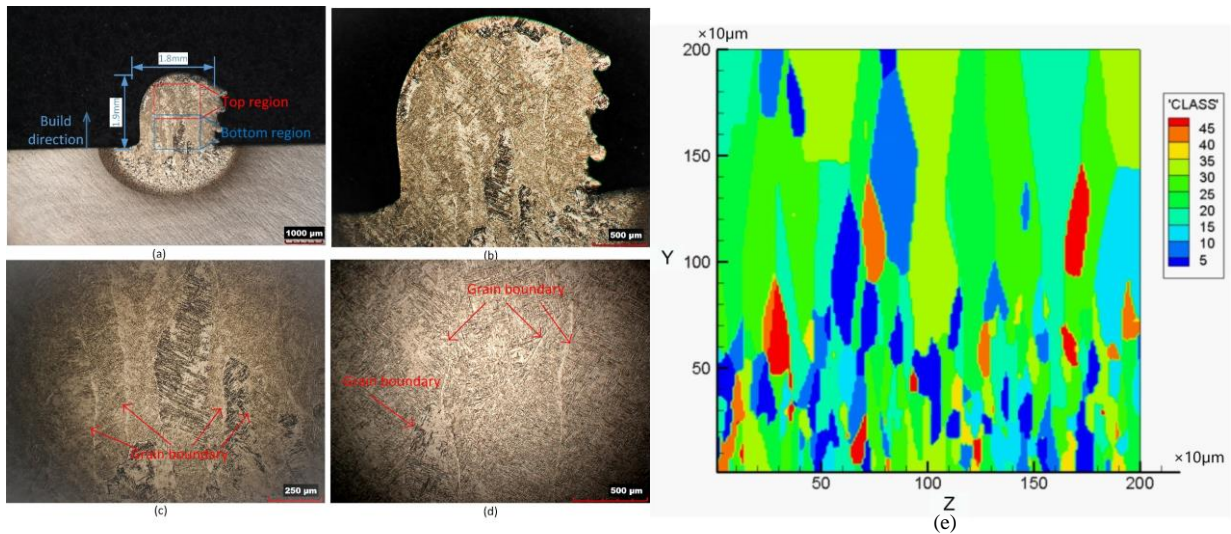


Figure 16. Ti-6Al-4V deposition grain morphologies. (a)(b) the whole deposition (c) the bottom region deposition (d) the top region deposition. (e) Grain morphology modeling of 25-layer Ti-6Al-4V laser deposition. In the legend, ‘CLASS’ represents orientations of different grains. Y and Z coordinates are in agreement with 25-layer thermal history result

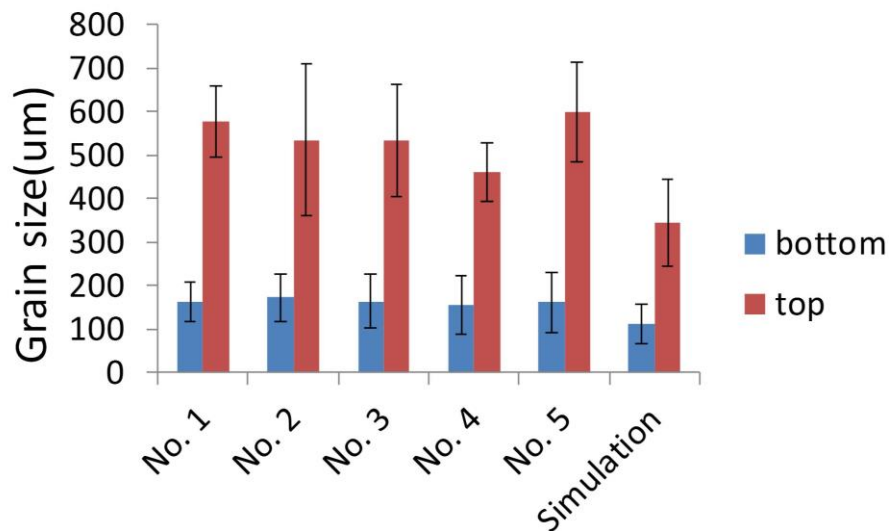


Figure 17. Grain size comparison of multiple layers between simulation and experiment

#### 4 Conclusions

The transient temperature field of one-layer and multiple-layer deposition of Ti-6Al-4V was simulated with finite element method. The simulation result was validated by thermocouple experiment. The FE model provides the temperature at a relatively coarse scale (200µm) and interpolation algorithm was used to scale the temperature field to match that of the CA model. The FE-CA model predicts grain morphology evolution as the deposition cools down. Hence, the instantaneous nucleation law, grain growth, and crystallographic orientation were modeled in this study. It has been found that the developed “decentered polygon” growth method is

more appropriate for the highly non-uniform temperature field, and the simulation result is more closed to the real experimental measurement compared to conventional growth method. For multi-layer deposit, columnar grains dominated in the 25-layer deposition in the simulation. The grain size becomes larger when the position is closer to the top area of the deposition, which matches well with the optical microscopic result. The grain size of single layer and multiple layer between simulation and experiment are similar. It demonstrates that this FE-CA simulation can reasonably predict thermal history and grain morphology during this case of Direct Metal Deposition.

## 5 Acknowledgement

This work was funded through NASA's Fundamental Aeronautics Program, Fixed Wing Project, under NRA NNX11AI73A.

## References

- [1] Rappaz, M., 1989, "Modelling of microstructure formation in solidification processes no," **34**(3).
- [2] Anderson, M. ., Srolovitz, D. ., Grest, G. ., and Sahni, P. ., 1984, "Computer simulation of grain growth—I. Kinetics," *Acta Metall.*, **32**(5), pp. 783–791.
- [3] Srolovitz, D. J., Anderson, M. P., Sahni, P. S., and Grest, G. S., 1984, "Computer simulation of grain growth—II. Grain size distribution, topology, and local dynamics," *Acta Metall.*, **32**(5), pp. 793–802.
- [4] Saito, Y., and Enomoto, M., 1992, "Monte Carlo Simulation of Grain Growth," *ISIJ Int.*, **32**(3), pp. 267–274.
- [5] Chen, L.-Q., 2002, "PHASE-FIELD MODELS FOR MICROSTRUCTURE EVOLUTION."
- [6] Krill III, C. E., and Chen, L.-Q., 2002, "Computer simulation of 3-D grain growth using a phase-field model," *Acta Mater.*, **50**(12), pp. 3059–3075.
- [7] Böttger, B., Eiken, J., and Steinbach, I., 2006, "Phase field simulation of equiaxed solidification in technical alloys," *Acta Mater.*, **54**(10), pp. 2697–2704.
- [8] Moelans, N., Blanpain, B., and Wollants, P., 2008, "An introduction to phase-field modeling of microstructure evolution," *Calphad*, **32**(2), pp. 268–294.
- [9] Rappaz, M., and Gandin, C.-A., 1993, "Probabilistic modelling of microstructure formation in solidification processes," *Acta Metall. Mater.*, **41**(2), pp. 345–360.
- [10] Gandin, C.-A., and Rappaz, M., 1994, "A coupled finite element-cellular automaton model for the prediction of dendritic grain structures in solidification processes," *Acta Metall. Mater.*, **42**(7), pp. 2233–2246.

- [11] Gandin, C.-A., Desbiolles, J.-L., Rappaz, M., and Thevoz, P., 1999, "A three-dimensional cellular automation-finite element model for the prediction of solidification grain structures," *Metall. Mater. Trans. A*, **30**(12), pp. 3153–3165.
- [12] Choudhury, A., Reuther, K., Wesner, E., August, A., Nestler, B., and Rettenmayr, M., 2012, "Comparison of phase-field and cellular automaton models for dendritic solidification in Al–Cu alloy," *Comput. Mater. Sci.*, **55**, pp. 263–268.
- [13] Dore, X., 2000, "MODELLING OF MICROSEGREGATION IN TERNARY ALLOYS: APPLICATION TO THE SOLIDIFICATION OF Al–Mg–Si ' 1 \*," **48**, pp. 3951–3962.
- [14] Jarvis, D. J., Brown, S. G. R., and Spittle, J. A., 2000, "Modelling of non-equilibrium solidification in ternary alloys : comparison of 1D , 2D , and 3D cellular automaton ± ® nite difference simulations," **16**(December), pp. 2–6.
- [15] Grujicic, M., Cao, G., and Figliola, R. S., 2001, "Computer simulations of the evolution of solidification microstructure in the LENS TM rapid fabrication process," **183**, pp. 43–57.
- [16] Kelly, S. M., and Kampe, S. L., 2004, "Microstructural evolution in laser-deposited multilayer Ti-6Al-4V builds: Part II. Thermal modeling," *Metall. Mater. Trans. A*, **35**(6), pp. 1869–1879.
- [17] Kelly, S. M., and Kampe, S. L., "Microstructural evolution in laser-deposited multilayer Ti-6Al-4V builds: Part I. Microstructural characterization," *Metall. Mater. Trans. A*, **35**(6), pp. 1861–1867.
- [18] Lütjering, G., 1998, "Influence of processing on microstructure and mechanical properties of ( $\alpha$ + $\beta$ ) titanium alloys," *Mater. Sci. Eng. A*, **243**(1–2), pp. 32–45.
- [19] Reddy, J. N., and Gartling, D. K., 2010, *The finite element method in heat transfer and fluid dynamics*, CRC Press LLC.
- [20] Phillips, L. C. A. R. L., 2005, *Laser Beam Propagation through Random Media*, SPIE Publications.
- [21] Alimardani, M., Toyserkani, E., and Huissoon, J. P., 2007, "A 3{D} dynamic numerical approach for temperature and thermal stress distributions in multilayer laser solid freeform fabrication process," *Opt. Lasers Eng.*, **45**(12), pp. 1115–1130.
- [22] Lampa, C., Kaplan, A. F. H., Powell, J., and Magnusson, C., 1997, "An analytical thermodynamic model of laser welding," *J. Phys. D. Appl. Phys.*, **30**(9), p. 1293.
- [23] Liu, H., and Sparks, T., 2012, "MODELING AND VERIFICATION OF TEMPERATURE DISTRIBUTION AND RESIDUAL STRESS IN LASER AIDED METAL DEPOSITION PROCESS," (1), pp. 1–7.
- [24] Oldfield, W., 1966, "A quantitative approach to casting solidification: Freezing of cast iron," *Trans. Am. Soc. Met.*, **59**, p. 945.

[25] D.J.FISHER, W. K. and, 1992, “Appendix 7 and 8,” Fundamentals of Solidification, TRANS TECH PUBLICATION, pp. 226–246.

[26] D.J.FISHER, W. K. and, 1992, “Appendix 9,” Fundamentals of Solidification, TRANS TECH PUBLICATION, pp. 247–260.

[27] Chen, R., Xu, Q., and Liu, B., 2014, “A Modified Cellular Automaton Model for the Quantitative Prediction of Equiaxed and Columnar Dendritic Growth,” J. Mater. Sci. Technol., **30**(12), pp. 1311–1320.